

FIRST PERFORMANCE STUDIES OF A PROTOTYPE  
FOR THE CASTOR FORWARD CALORIMETER  
AT THE CMS EXPERIMENT

X. ASLANOGLU<sup>a</sup>, A. CYZ<sup>b</sup>, N. DAVIS<sup>c</sup>, D. D'ENTERRIA<sup>d</sup>  
E. GLADYSZ-DZIADUS<sup>b</sup>, C. KALFAS<sup>e</sup>, Y. MUSIENKO<sup>f</sup>  
A. KUZNETSOV<sup>f</sup>, A.D. PANAGIOTOU<sup>c</sup>

<sup>a</sup>University of Ioannina, P.O. Box 1186, 45110 Ioannina, Greece

<sup>b</sup>Institute of Nuclear Physics, Radzikowskiego 152, 31342 Kraków, Poland

<sup>c</sup>University of Athens, Phys. Dept. 15701 Athens, Greece

<sup>d</sup>CERN, PH Dept., 1211 Geneva 23, Switzerland

<sup>e</sup>NRC "Demokritos" INP, P.O. Box 60228, 15310 Ioannina, Greece

<sup>f</sup>Northeastern University, Dept. of Physics, Boston, MA 02215, USA

(Received February 15, 2008)

We present results on the performance of the first prototype of the CASTOR quartz-tungsten sampling calorimeter, to be installed in the very forward region of the CMS experiment at the LHC. This study includes GEANT Monte Carlo simulations of the Cherenkov light transmission efficiency of different types of air-core light guides, as well as analysis of the calorimeter linearity and resolution as a function of energy and impact-point, obtained with 20–200 GeV electron beams from CERN/SPS tests in 2003. Several configurations of the calorimeter have been tested and compared, including different combinations of *(i)* structures for the active material of the calorimeter (quartz plates and fibres), *(ii)* various light-guide reflecting materials (glass and foil reflectors) and *(iii)* photodetector devices (photomultipliers and avalanche photodiodes).

PACS numbers: 25.75.-q, 12.38.Mh, 29.40.Vj

## 1. Introduction

Heavy ion experiments at CERN LHC will be mainly concentrated and fully instrumented for hadron and photon identification in the acceptance region of  $|\eta| < 2.5$  around mid-rapidity [1] covering only part of the total phase space, which at the beam energy of 2.75 ATeV for Pb ions at LHC, extends to  $|\eta| = 8.7$ . Therefore, in addition to the main detector systems some smaller detectors, covering the forward rapidity region, are planned to be installed.

Already at the early stage of the preparation of the physics motivation for the heavy ion studies at the LHC, it was pointed out [2] that the interesting physics beyond midrapidity should be the additional subject of the investigations. Some theoretical considerations as well as the results of cosmic ray experiments indicate the forward rapidity baryon-rich environment as a potentially very rich field of novel phenomena. High energy cosmic ray interactions show the existence of a wide spectrum of Centauro-type unusual events, revealing many surprising features, such as: abnormal hadron dominance, transverse momentum of produced particles much higher than that observed in “normal” interactions, the existence of mini-clusters *etc.* [3]. In addition, they are very frequently connected with the so-called long-flying (penetrating) component [4]. Many models have been developed to understand these anomalies [4], but only the strange quark matter (SQM) model [5], supplemented with the idea of formation and passage of strangelets (small nuggets of quark matter with approximately the same number of  $u$ ,  $d$  and  $s$  quarks) through matter [6], explains simultaneously both the Centauro-type species and the strongly penetrating component.

The important question is the existence and the properties of the Quark Gluon Plasma (QGP) state. The theoretical considerations suggest [7] that the phase diagram (temperature  $T$  *versus* chemical potential of quark  $-\mu_q$ ) features a critical endpoint at which the line of the first order phase transition ends. Passing close enough to this point should have characteristic experimental consequences. Since one can miss the critical point on either of two sides a nonmonotonic dependence of the control parameters can be expected. It is the reason that the novel phenomena are expected to appear in the dense baryon environment produced in Pb+Pb collisions at LHC energies, in particular the formation of Deconfined Quark Matter (DQM), with characteristics different from those expected in the much higher temperature baryon-free region around midrapidity. Exploration of this kinematic region, can provide unique investigations of the baryochemical-potential dependence on the properties of the QGP.

The idea of the CASTOR (Centauro And STrange Object Research) detector evolved from these considerations [8]. The novel tungsten/quartz electromagnetic (EM) and hadronic (HAD) calorimeter of about  $10.0 \lambda_i$  and with fine azimuthal (16 sectors) and longitudinal (14 segments) segmentation will be a unique apparatus, capable to study the anomalous transition curves (depth and energy fluctuations) in the development of hadronic showers. The anomalous energy deposition pattern in the deep calorimeters, has been proposed as the new signature of the exotic events, such as strangelets, Centauros, DCC [9, 10].

As the LHC, with an energy equivalent to  $\sim 10^{17}$  eV for a moving proton impinging on one at rest, will be the first accelerator to effectively probe the highest cosmic energy domain, the investigation of the anomalous cosmic-ray events [11], as well as the tuning and calibration of Monte-Carlo codes, used for interpretation of ultra-high energy cosmic-ray data, are the primary aims of CASTOR. The simulations showed that the CASTOR calorimeter is suitable to search and identify charged as well as neutral strangelets, despite of their lifetime.

The wide programme concerning nucleus–nucleus ( $AA$ ), proton–nucleus ( $pA$ ) as well as  $pp$  physics at the forward rapidity region has been intensively developed [12] for the CASTOR detector and now goes well beyond the study of cosmic-ray related phenomena.

Forward physics program includes a broad range of high energy physics topics, from fundamental properties of Quantum Chromo-Dynamics to new physics phenomena and the determination of the luminosity. Among many others, such subjects as low- $x$  QCD physics, diffractive QCD processes will be studied with CASTOR. The nonperturbative region of QCD at Bjorken- $x$  as small as  $\sim 10^{-6}$ – $10^{-7}$  and the Color Glass Condensate for which there is some evidence at HERA and RHIC data will be investigated.

With the design specifications for CASTOR, the total and the electromagnetic energies in its acceptance range ( $\sim 170$  TeV and  $\sim 50$  TeV respectively, according to Hijing [13] PbPb simulations at 5.5 TeV) can be measured with a resolution below  $\sim 1\%$  and, therefore, “Centauro” and/or strangelets events with an unusual ratio of electromagnetic to total (hadronic) energies can be well identified.

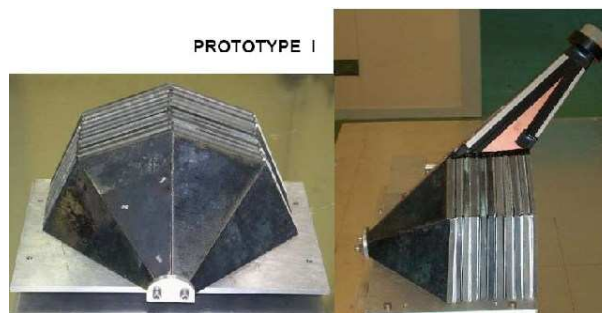


Fig.1. CASTOR prototype I: frontal view (left picture) and lateral view (right picture, only one light guide is shown).

The first prototype of the CASTOR calorimeter has been constructed and tested with electron beams at CERN/SPS in the summer 2003. The purpose of this beam test was to investigate and compare the performance of different component options (structure of the quartz active material, choice

of the light guides/reflectors and photodetector devices), rather than to obtain precise quantitative results of the response of the final detector setup. The general view of the prototype is shown in Fig. 1. The different detector configurations considered in this work are shown schematically in Fig. 2. Preliminary results of the analysis have been presented at different CMS meetings [14]. Here we present a more quantitative analysis, including the beam profile data [15].

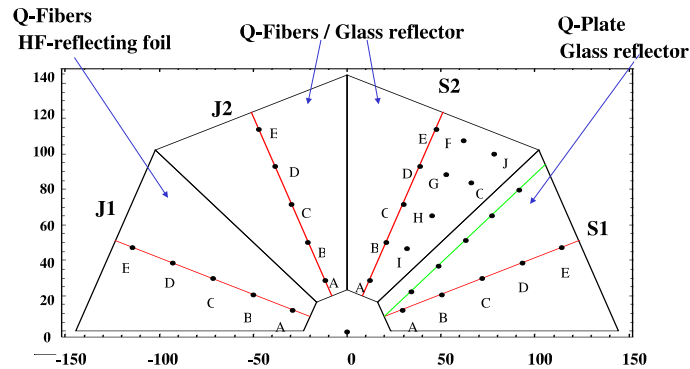


Fig. 2. Configuration options investigated in the 2003 beam test: different quartz structures (fibres and plate) and reflectors (glass, foil). The points A–O and 4–8 are scan locations used in calorimeter response uniformity studies (see Sec. 3.2),  $x$ – $y$  units are mm.

## 2. Technical description

The CASTOR detector is a Cherenkov-effect based calorimeter with tungsten (W) absorber and quartz (Q) as sensitive material. An incident high-energy particle will shower in the tungsten volume and produce relativistic charged particles that will emit Cherenkov light in the quartz plane. The Cherenkov light is then collected and transmitted to photodetector devices through air-core light-guides. The different instrumentation options, investigated in this work, are shown in Fig. 2. In Sec. 2.1 we describe the various arrangements of the active (quartz) and passive (tungsten) materials of the calorimeter considered. Sec. 2.2 discusses the light transmission efficiency of different light-guide geometries, Sec. 2.3 compares two different light-guide reflecting materials, and Sec. 2.4 summarizes the characteristics of the photodetectors (photomultipliers and avalanche photodiodes) tested.

### 2.1. Tungsten–quartz

The calorimeter prototype is azimuthally divided into 4 octants and longitudinally segmented into 10 W/Q layers (Fig. 1). Each tungsten absorber layer is followed by a number of quartz planes. The tungsten/quartz planes are inclined at  $45^\circ$  with respect to the beam axis to maximize Cherenkov light output<sup>1</sup>. The effective length of each W-plate is 7.07 mm, being inclined at  $45^\circ$ . The total length is calculated to be  $0.73\lambda_{\text{int}}$  and  $19.86X_0$ , taking a density for the used W-plates of  $\sim 19.0 \text{ g/cm}^3$  and ignoring the contribution of the quartz material.

The calorimeter response and relative energy resolution were studied for quartz fibres (QF) and quartz plates (QP) (see Sec. 3). We have tested four octant readout units of the calorimeter, arranged side-by-side in four azimuthal sectors. Each readout unit consisted of 10 sampling units. Each sampling unit for sectors J1, J2, and S2 (see Fig. 2) is comprised of a 5 mm thick tungsten plate and three planes of 640  $\mu\text{m}$  thick quartz fibres. The quartz fibres were produced by Ceram Optec and have 600  $\mu\text{m}$  pure fused silica core with a 40  $\mu\text{m}$  polymer cladding and a corresponding numerical aperture  $\text{NA} = 0.37$  (in general, an optical fibre consists of the core with index of refraction  $n_{\text{core}}$ , and the cladding with index  $n_{\text{clad}}$ , and  $\text{NA} = \sqrt{n_{\text{core}}^2 - n_{\text{clad}}^2}$ ). The sampling unit for sector S1 consisted of a 5 mm thick tungsten plate and one 1.8 mm thick quartz plate. Both types of quartz active material, fibre or plate, had about the same effective thickness. The filling ratio was 30% and 37% for the quartz fibres and quartz plates, respectively. Simulations showed [14] that the energy resolution of the calorimeter with such values of filling ratios will be reasonable and it will produce the sufficient flux of Cherenkov photons.

### 2.2. Air-core light guides

The light guide constructed for the CASTOR prototype I is shown in Fig. 3. It is an air-core light-guide made of Cu-plated 0.8 mm PVC (the internal walls are covered either with a glass reflector or with a reflector foil, which are compared in the next section). In this section the optimal design and dimensions of the light guide are obtained based on detailed GEANT Monte Carlo simulations.

In the simulations, the Cherenkov photons produced in the quartz of the calorimeter are collected and transmitted to the photodetectors by air-core light guides. The efficiency of light transmission and its dependence on

---

<sup>1</sup> The index of refraction of quartz is  $n = 1.46\text{--}1.55$  for wavelengths  $\lambda = 600\text{--}200 \text{ nm}$ . The corresponding Cherenkov threshold velocity is  $\beta_c = 1/n = 0.65\text{--}0.69$ , and therefore, for  $\beta_c \approx 1$  the angle of emission is  $\theta_c = \arccos(1/n\beta) = 46^\circ\text{--}50^\circ$ .

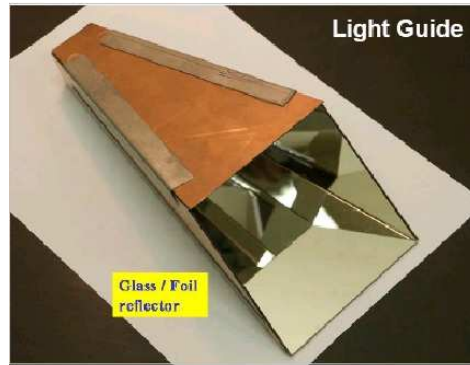


Fig. 3. Picture of the light guide used in the prototype.

the light-source position are crucial parameters characterizing the light guide and significantly affecting the performance of the calorimeter. We developed a GEANT 3.21-based code to simulate the transmission of Cherenkov photons produced in the quartz plane through a light guide [16]. A photon is tracked until it is either absorbed by the walls or by the medium and is thus lost, or until it escapes from the light guide volume. In the latter case it is considered detected only if it escapes through the exit to the photodetector. If it is back-scattered towards the entry of the light guide it is also lost.

Inside the fibre core Cherenkov photons are practically produced isotropically. But those that are captured and propagate through the lightguide have an exit angle with respect to the fibre longitudinal axis up to a maximum value ( $\theta_{\text{core}}$ ) which depends on the numerical aperture NA and the core refraction index ( $n_{\text{core}}$ ). When traversing the core-air boundary at the entrance of the lightguide, the photons undergo refraction resulting in a larger angle ( $\theta_{\text{air}}$ ). In the simulations, fibres of various numerical apertures ( $\text{NA} = 0.22\text{--}0.48$ ) as well as light-guides of various shapes (fully square cross section or partially tapered) were used (see Fig. 4). The maximum values

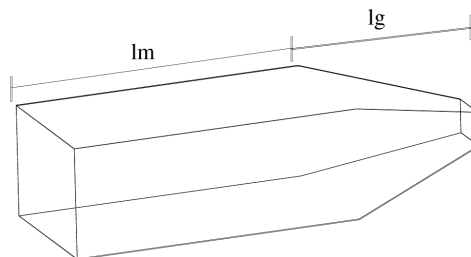


Fig. 4. Schematic view of the air-core light guide geometry.  $lg$  ( $lm$ ) is defined as the ratio of the length of the (non-)tapered section over the width of the entrance plane (assumed to be unity in the figure).

of core-exiting and air-entering angles ( $\theta_{\text{core}}$ ,  $\theta_{\text{air}}$ ) in degrees for various numerical apertures are given in Table I. For the quartz plate, the air-entering angle,  $\theta_{\text{air}}$ , is larger than  $30^\circ$ .

TABLE I

Maximum values of the core-exiting ( $\theta_{\text{core}}$ ) and air-exiting ( $\theta_{\text{air}}$ ) angles, for various numerical apertures (NA) of the quartz fibres (index of refraction:  $n_{\text{core}} = 1.46$ ).

NA ( $n_{\text{core}}=1.46$ )	$\theta_{\text{core}}$	$\theta_{\text{air}}$
0.22	8.7	12.7
0.37	14.7	21.7
0.40	15.9	23.6
0.44	17.5	26.1
0.48	19.2	28.7

The walls of the GEANT light-guide have a reflection coefficient of 0.85 (simulating the transmittance of the reflecting internal mirror surface and the quantum efficiency of the photodetector devices, see next section and Table VI). The entrance plane of the light guide was uniformly scanned with the simulated light source. The percentage of photons escaping in the direction of the photodetector has been recorded as a function of the source position, giving, after integration over the complete surface, the light guide efficiency. The spatial uniformity of the light-guide performance can be quantified with the relative variation ( $\sigma/\text{mean}$ ) of the efficiency across the entrance. Results for the light guides efficiency and uniformity studied are tabulated<sup>2</sup> in Tables I–V and are plotted in Figs. 5 and 6 for fibres with NA = 0.37 and 0.48, respectively.

We studied air-core lightguides of square cross section (with entrance area  $10 \times 10 \text{ cm}^2$ ), fully or partially tapered. The parameters  $lg$  and  $lm$  refer to the tapered and non-tapered sections of the light guide, as shown in Fig. 4, defined as [16]:

$lg$  = ratio of the length of the tapered part over the width of the entrance plane, and

$lm$  = ratio of the length of non tapered part over the width of the entrance plane.

<sup>2</sup> Note, that only the points relevant for the actual light-guide construction are included in the table.

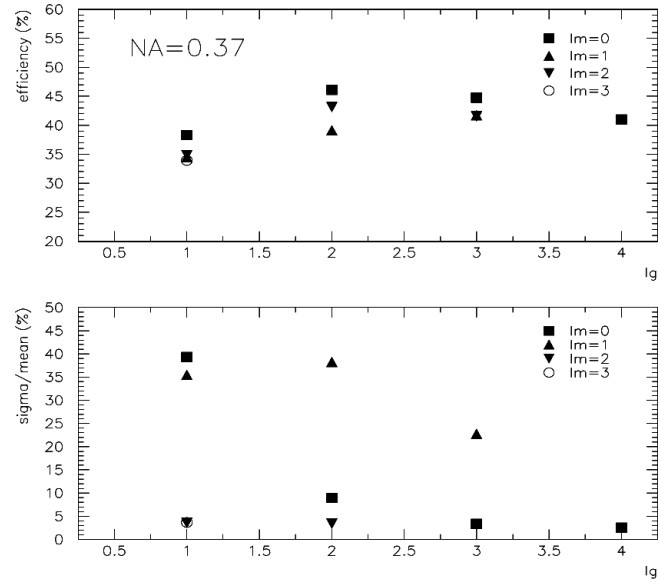


Fig. 5. Efficiency (top) and relative variation of the efficiency (bottom) for various light guides (calorimeter quartz fibres with  $NA = 0.37$ ) for different values of the  $lg$  and  $lm$  parameters (see text).

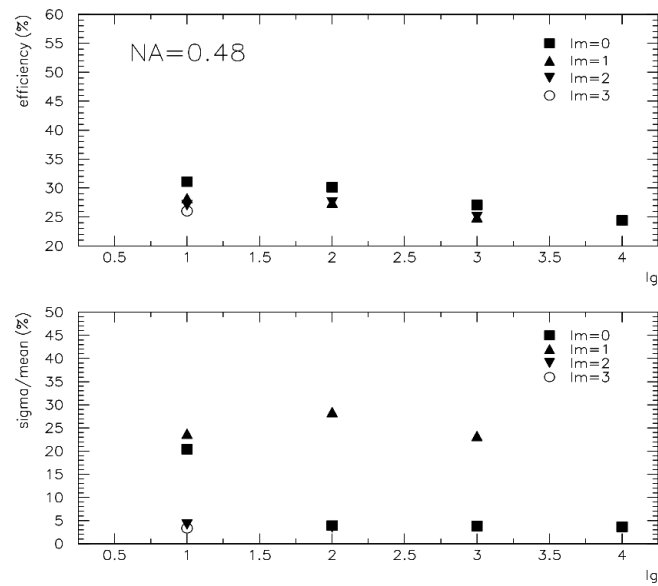


Fig. 6. Efficiency (top) and relative variation of the efficiency (bottom) for various light guides (calorimeter quartz fibres with  $NA = 0.48$ ) for different values of the  $lg$  and  $lm$  parameters (see text).



Thus, *e.g.* with a mean entrance length of 10 cm, a value  $lg : lm = 1 : 2$  indicates that the light-guide has a total length of 30 cm with 10 cm of tapering part, and a value  $lg : lm = 2 : 0$  indicates a fully tapered light-guide with length 20 cm, and so on. In Tables II–V, the row (column) indicates the magnitude of the parameters  $lm$  ( $lg$ ), respectively.

TABLE II

Light-guide efficiency (%) for different values of the  $lg$  and  $lm$  parameters (see text) and quartz fibres with  $NA = 0.37$ .

$lg \backslash lm$	0	1	2
1	38.3	34.5	34.8
2	46.1	39.1	43.2
3	44.8	41.8	41.5

TABLE III

Relative variation of the light-guide efficiency across the entrance,  $\sigma/\text{Mean}$  (%), for different values of the  $lg$  and  $lm$  parameters (see text) and quartz fibres with  $NA = 0.37$ .

$lg \backslash lm$	0	1	2
1	39.3	35.5	3.6
2	8.9	38.3	3.4
3	3.3	22.8	3.2

TABLE IV

Light-guide efficiency (%) for different values of the  $lg$  and  $lm$  parameters (see text) and quartz fibres with  $NA = 0.48$ .

$lg \backslash lm$	0	1	2
1	31.1	28.3	27.1
2	30.1	27.5	27.5
3	27.1	25.0	25.0

TABLE V

Relative variation of the light-guide efficiency across the entrance,  $\sigma/\text{Mean}$  (%), for different values of the  $lg$  and  $lm$  parameters (see text) and quartz fibres with  $\text{NA} = 0.48$ .

$lg \backslash lm$	0	1	2
1	20.4	23.8	4.1
2	3.9	28.4	4.6
3	3.8	23.2	3.7

From Tables I–V and Figs. 5 and 6 we note that, as the NA of the fibre and hence the air-entering angle,  $\theta_{\text{air}}$ , increases, the transmission efficiency decreases. Also, the optimum length for the air-core light guide decreases, while the uniformity of the light exiting increases. In order to obtain an optimum efficiency and uniformity of light transmission within the realistically available space, the best option seems  $lm = 0$  and  $lg = 2$  for  $\text{NA} = 0.37$  and  $0.48$ . A more detailed study of the light guide performances — beyond the scope of our current paper — can be found in reference [16].

### 2.3. Light guide reflecting material

The light transmittance in the light-guides was studied for two alternatives for the reflecting medium:

1. 0.5 mm thick float-glass with evaporations of AlO and MgFr (Fig. 7, left) and
2. Dupont polyester film reflector coated with AlO and reflection enhancing dielectric layer stack  $\text{SiO}_2 + \text{TiO}_2$ , the so-called HF reflector foil (Fig. 7, right).

TABLE VI

Light guide transmittance times the Avalanche Photodiode quantum efficiency at each wavelength (see Figure 9) for the two reflectors considered (in both cases the quartz fibres have  $\text{NA} = 0.37$  and 3 internal reflections).

Wavelength	Glass reflector (Al+MgF)	Dupont + Layer stack
650 nm	62%	64%
400 nm	53%	62%
350 nm	44%	7%
300 nm	10%	$\sim 0\%$

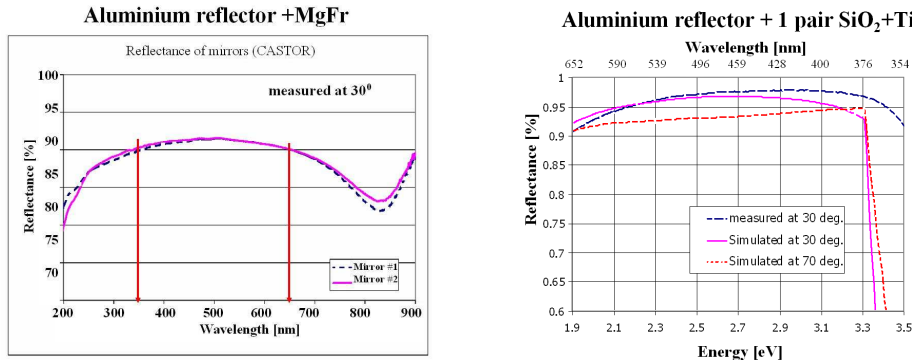


Fig. 7. Reflectance of two mirrors coated with AlO+MgFr (left) and Dupont foil with AlO and SiO<sub>2</sub>+TiO<sub>2</sub> (right), as a function of the incident light wavelength.

To choose the most suitable reflector, we also have to take into account the quantum efficiency of the photodetector device (see Sec. 2.4). In Table VI we calculate the product of the light guide transmittance and Avalanche Photodiodes (APD) quantum efficiency for Q-fibres with NA = 0.37 and 3 internal reflections in the designed light guide. The light output is higher (lower) for the light-guides with reflector-foil (glass-reflector) for wavelengths above (below)  $\lambda = 400$  nm. We prefer the HF-reflector solution since the short wavelength Cherenkov light ( $\lambda < 400$  nm) deteriorates fast with irradiation of the quartz material and thus a continuous compensation must be applied [17]. The optimum combination of the HF-reflector and the Q-efficiency of the photodetector ensures that the total efficiency is maximized above 400 nm and falls sharply to zero below 400 nm.

#### 2.4. Photodetectors

We instrumented the calorimeter prototype with two different types of light-sensing devices:

1. Two different kinds of Avalanche Photodiodes (APDs): Hamamatsu S8148 (APD1, developed for the CMS electromagnetic calorimeter [18]) and Advanced Photonix Deep-UV (APD2), Fig. 8.
2. Two different types of photomultipliers (PMTs): Hamamatsu R374 and Philips XP2978.

We used 4 Hamamatsu APDs, each  $5 \times 5$  mm<sup>2</sup>, in a  $2 \times 2$  matrix with total area of 1 cm<sup>2</sup>. The Advanced Photonix DUV APD had an active area of 2 cm<sup>2</sup> (16 mm diameter). The Hamamatsu and Philips PMTs have both an active area of 3.1 cm<sup>2</sup>. The Hamamatsu and Advanced Photonix APD quantum efficiencies are shown *versus* wavelength in Fig. 9.



Fig. 8. The two types of APDs used in the beam test: Hamamatsu S8148 (left,  $5 \times 5 \text{ mm}^2$ , in a  $2 \times 2$  matrix with total  $1 \text{ cm}^2$  active area) and Advanced Photonix DUV (right, active area of  $2 \text{ cm}^2$ ).

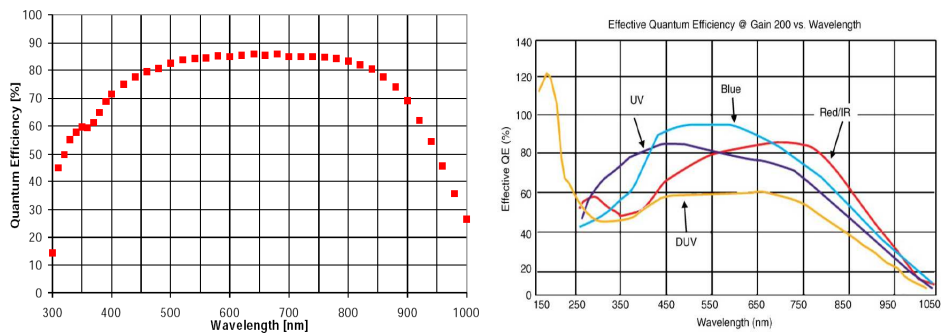


Fig. 9. APDs quantum efficiencies *versus* wavelength: Hamamatsu S8148 (left) and Advanced Photonix (right, the curve labeled 'blue' is relevant for this study).

### 3. Beam test results

The beam test took place in summer 2003 at the H4 beam line of the CERN SPS. The calorimeter prototype was placed on a platform movable with respect to the electron beam in both horizontal and vertical ( $X, Y$ ) directions. Telescopes of two wire chambers, as well as two crossed finger scintillator counters, positioned in front of the calorimeter, were used to determine the electron impact point. In the next two sections we present the measured calorimeter linearity and resolution as a function of energy and impact point for different prototype configurations.

### 3.1. Energy linearity and resolution

To study the linearity of the calorimeter response and the relative energy resolution as a function of energy, the central points C (Fig. 2) in different azimuthal sectors have been exposed to electron beams of energy 20, 40, 80, 100, 150 and 200 GeV. The results of the energy scanning, analyzed for four calorimeter configurations, are shown in Figs. 10–13. The distributions of signal amplitudes, after introducing the cuts accounting for the profile of the beam, are symmetric and well fitted by a Gaussian function.

For all configurations, the calorimeter response is found to be linear in the energy range explored (see Fig. 14). The average signal amplitude, expressed in units of ADC channels, can be satisfactorily fitted by the following formula:

$$\text{ADC} = a + b \times E, \quad (1)$$

where the energy  $E$  is in GeV. The fitted values of the parameters for each configuration are shown in Fig. 14 and are tabulated in Table VII. The values of the intercept 'a' are consistent with the position of the ADC pedestal values measured for the various configurations considered:  $36.1 \pm 0.3$  (S1-Quartz Plate),  $38.4 \pm 1.8$  (S2-Quartz Fibres),  $35.3 \pm 1.5$  (J2-Quartz Fibres, glass reflector),  $35.4 \pm 0.6$  (J1-Quartz Fibres, foil reflector).

The relative energy resolution of the calorimeter has been studied by plotting the normalized width of the Gaussian signal amplitudes (Figs. 10–13),  $\sigma/E$ , with respect to the incident beam electron energy,  $E$  (GeV) and fitting the data points with two different functional forms [19]:

$$\sigma/E = p_0 + p_1/\sqrt{E}, \quad (2)$$

$$\sigma/E = p_0 \oplus p_1/\sqrt{E} \oplus p_2/E, \quad (3)$$

where the  $\oplus$  indicates that the terms have been added in quadrature. In expression (3), three terms determine the energy resolution:

1. The constant term  $p_0$ , coming from the gain variation with changing voltage and temperature, limits the resolution at high energies.
2. The dominant stochastic term  $p_1$ , due to intrinsic shower photon statistics.
3. The noise  $p_2$  term, which contains the noise contribution from capacitance and dark current.

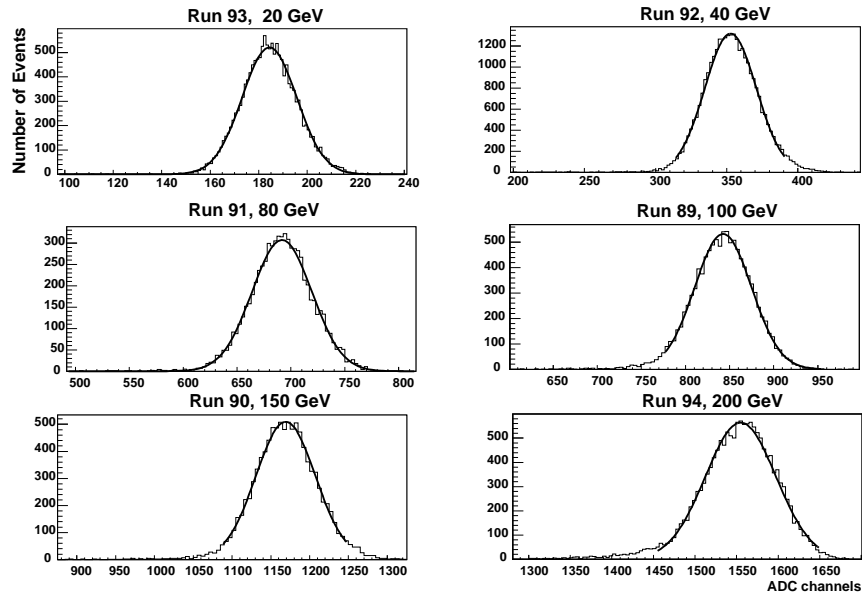


Fig. 10. Distributions of signal amplitudes in ADC channels for electron beam energies (20, 40, 80, 100, 150 and 200 GeV) impinging on the central point C of sector S1 (Quartz-Plate) using Philips PMT.

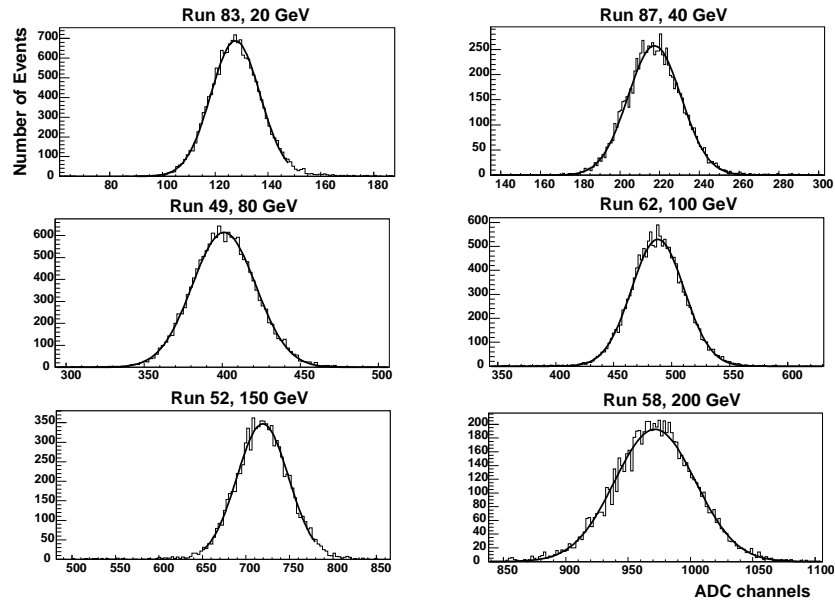


Fig. 11. Distributions of signal amplitudes in ADC channels for electron beam energies (20, 40, 80, 100, 150 and 200 GeV) impinging on the central point C of sector S2 (Quartz-Fibre) using Philips PMT.

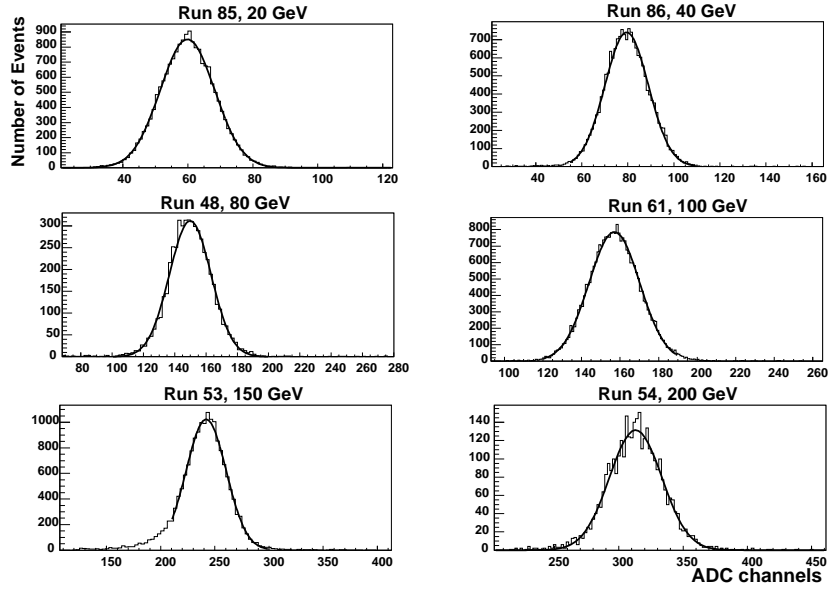


Fig. 12. Distributions of signal amplitudes in ADC channels for electron beam energies (20, 40, 80, 100, 150 and 200 GeV) impinging on the central point C of sector J2 (Quartz–Fibre) using Hamamatsu APD.

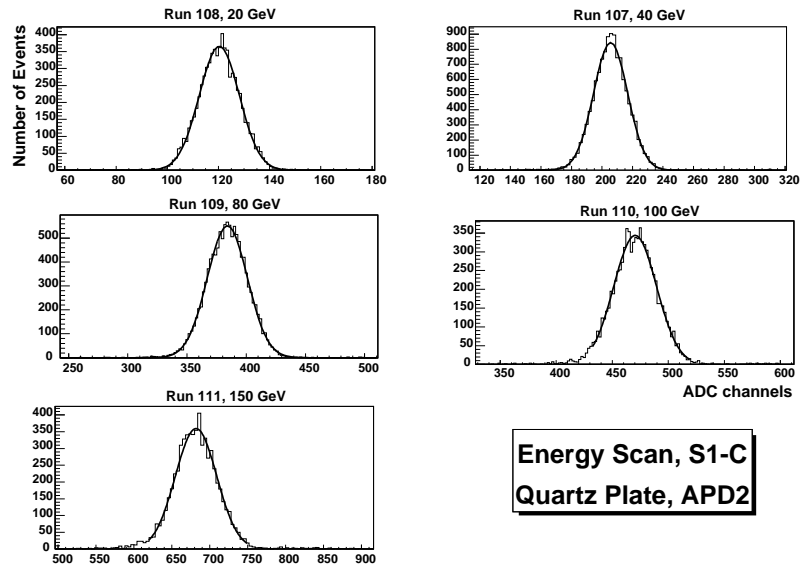


Fig. 13. Distributions of signal amplitudes in ADC channels for electron beam energies (20, 40, 80, 100, and 150 GeV) impinging on the central point C of sector S1 (Quartz–Plate) using Advanced Photonix APD.

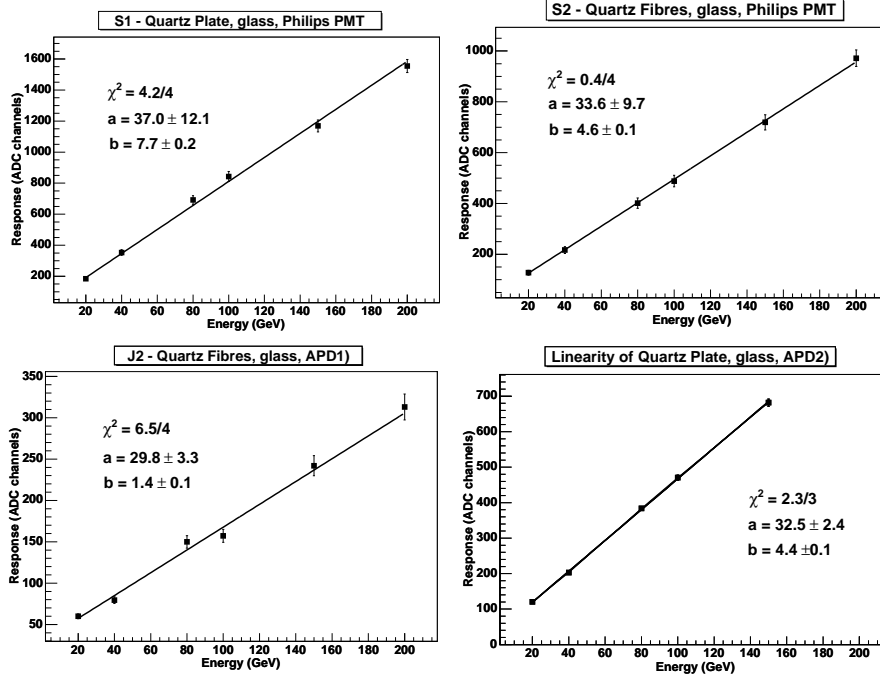


Fig. 14. Energy linearity in sectors: (top left) S1 (Philips PMT), (top right) S2 (Philips PMT), (bottom left) J2 (APD1), (bottom right) S1 (APD2).

Generally, both formulae satisfactorily fit the data (Fig. 15). The fit parameters are shown in Table VII. The first thing to notice is that the constant term  $p_0$  is close to 0 for all options. The average stochastic term  $p_1$  is in the range  $\sim 26\%$ – $96\%$  and indicates that we can measure the total Pb+Pb electromagnetic energy deposited in CASTOR at LHC energies ( $\sim 40$  TeV, according to Hijing [13]) with a resolution around 1%. The read-out by avalanche photodiodes leads to the  $p_2$  term, measured to be 1.25 GeV and 4.5 GeV for Advanced Photonix APD and Hamamatsu APD, respectively. It should be noted that the APDs are very sensitive to both voltage and temperature changes, but in this test there was no such stabilization. In Table VII we summarize the fit parameters for both parameterizations and for the four considered configurations.



TABLE VII

Energy linearity and resolution of four different configurations of the CASTOR calorimeter prototype. For the energy resolution, we quote the parameters for two fits: (1)  $\sigma/E = p_0 + p_1/\sqrt{E}$ , and (2)  $\sigma/E = p_0 \oplus p_1/\sqrt{E} \oplus p_2/E$  with  $E$  given in GeV.

	fit	Resolution			Linearity		
		$p_0$	$p_1$ (GeV <sup>1/2</sup> )	$p_2$ (GeV)	$a$	$b$ (GeV <sup>-1</sup> )	$\chi^2/ndf$
Quartz Plate (S1, glass) Philips PMT	(1)	0.004 ± 0.002	0.36 ± 0.02		37. ± 12.	7.7 ± 0.2	4.2/4
	(2)	0.010 ± 0.004	0.38 ± 0.02	0.0 ± 0.4			6.4/4 7.4/3
Adv. Photonix APD	(1)	0.017 ± 0.005	0.28 ± 0.04		32.5 ± 2.4	4.4 ± 0.1	2.5/3 2.2/3
	(2)	0.036 ± 0.006	0.24 ± 0.04	1.2 ± 0.2			6.2/2
Quartz Fibres (S2, glass) Philips PMT	(1)	0.004 ± 0.003	0.45 ± 0.04		33.6 ± 9.7	4.6 ± 0.1	3.2/4 0.41/4
	(2)	0.013 ± 0.006	0.48 ± 0.02	0.0 ± 0.8			3.7/3
Quartz Fibres (J2, glass) Adv. Photonix APD	(1)	-0.01 ± 0.01	1.16 ± 0.13		29.8 ± 3.3	1.4 ± 0.1	4.1/4 6.5/4
	(2)	0.04 ± 0.02	0.82 ± 0.22	4.5 ± 1.6			1.3/3

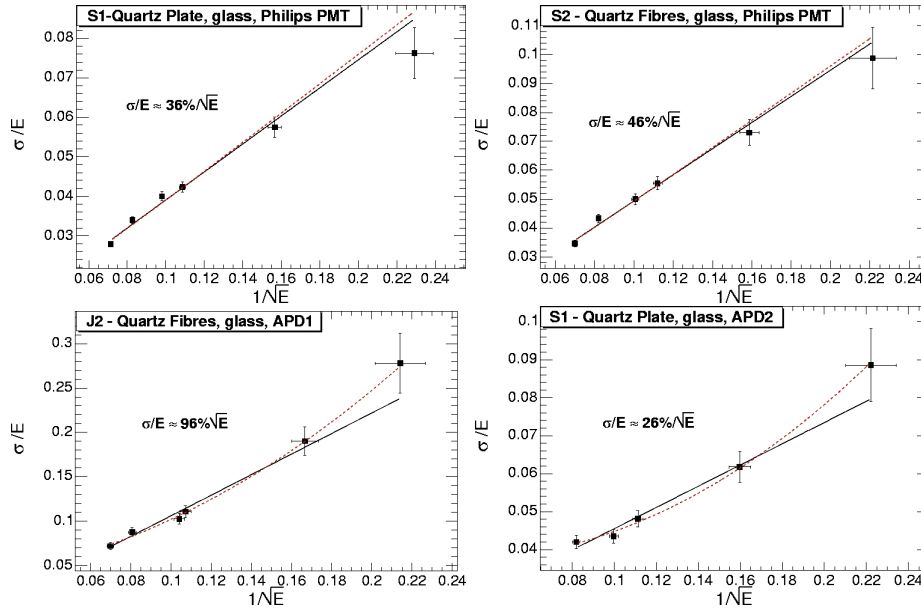


Fig. 15. Energy resolution in sectors: (top left) S1 (Philips PMT), (top right) S2 (Philips PMT), (bottom left) J2 (APD1), (bottom right) S1 (APD2). Two fits are shown:  $\sigma/E = p_0 + p_1/\sqrt{E}$  (solid);  $\sigma/E = p_0 + p_1/\sqrt{E} + p_2/E$  (dashed), with  $E$  given in GeV. The quoted  $\sigma/E$  values are an average between both fits.

### 3.2. Area scanning

The purpose of the area scanning was to check the uniformity of the calorimeter response, affected by electrons hitting points at different places on the sector area, as well as to assess the amount of “edge effects” and lateral leakage from the calorimeter, leading to cross-talk between neighbouring sectors.

For the area scanning of sector S2, connected to the Philips PMT, central points (A–E) as well as border points (I–O) have been exposed to electron beam of energy 100 GeV (see Fig. 2). The distributions are symmetric and well described by Gaussian fits for the majority of the points. Asymmetric distributions are seen only for points closer than  $\sim 3$  mm to the calorimeter outer edge or sector border.

Fig. 16 shows the calorimeter response and relative resolution ( $\sigma/E$ ) as a function of the distance  $R$  from the calorimeter center, for both central and border points. The top plot shows the coordinates of the points, corrected for the beam impact point position. It can be seen that points E, F, J practically lie at the upper edge of the calorimeter. The rise of the signal

amplitudes (bottom left), as well as of the distribution widths with  $R$  can be attributed to a lateral spread of the beam. For large  $R$ , a substantial part of the electron beam is outside of the calorimeter sector and falls directly onto the light guides. The bottom right plot shows that the energy resolution is  $\sim 4.7\%$  for 100 GeV electrons and is relatively independent of the position of the impact points.

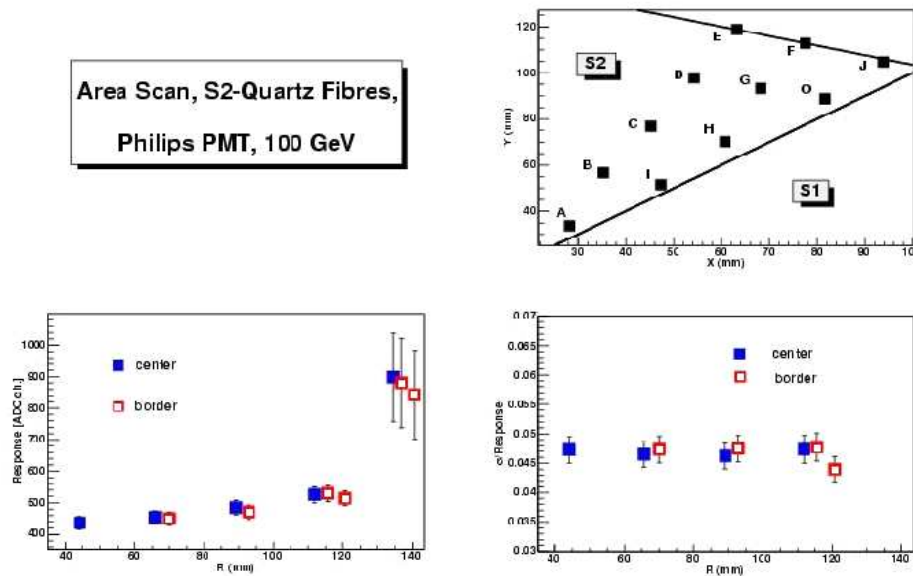


Fig. 16. Dependence of signal amplitude on the distance  $R$  from the calorimeter center in sector S2 (Philips PMT). Top: Coordinates of the scanned points. Bottom plots: Measured response to 100 GeV electrons on central (A–E, filled squares) and border (I–O, hollow squares) points.

### 3.2.1. S1–S2 cross talk

Ten points, located at distances 2.5–32 mm from the S1/S2 sector border, have been exposed to the electron beam of energy 80 GeV. The simultaneous readout of both sectors has been done by Advanced Photonix APD and Hamamatsu PMT in S1 and S2, respectively. The upper left pad of Fig. 17 shows the coordinates of the measured points in the calorimeter frame, corrected for the beam impact point position. The star symbol marks the coordinates of the border point between S1 and S2 sectors, found from the dependence of the signal amplitudes on  $X(Y)$  coordinates (lower pads).

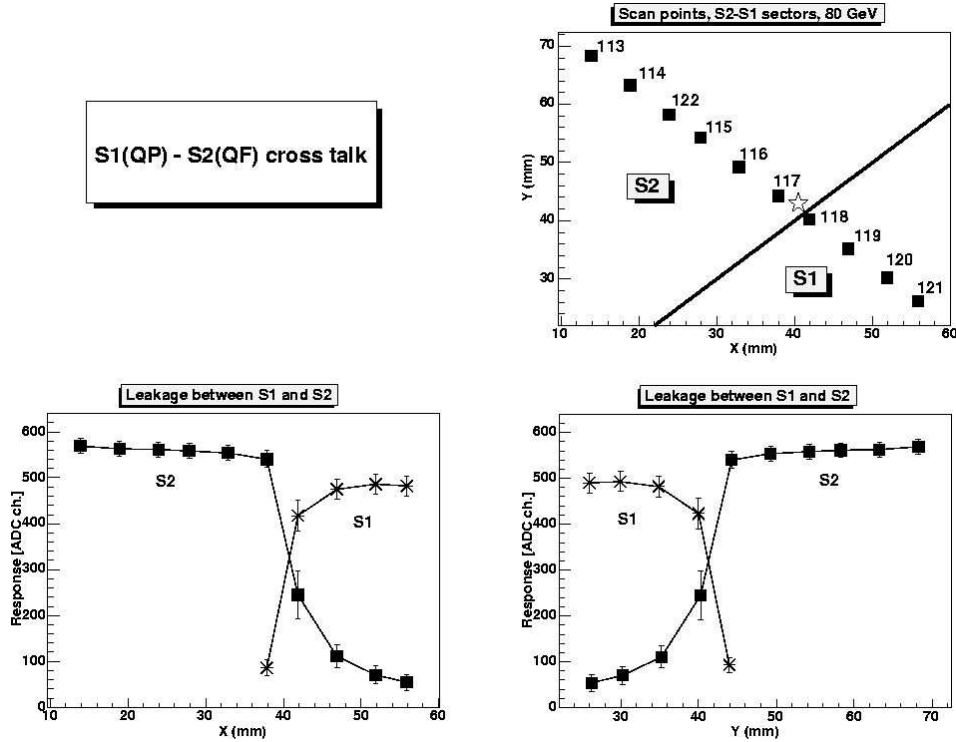


Fig. 17. Top: Position of the points in the calorimeter frame, corrected for the beam impact points. Bottom: Measured calorimeter response *versus* coordinates  $X$  (left) and  $Y$  (right) in sectors S1 (APD2) and S2 (Hamamatsu PMT) for several points at distances  $\sim 2.5$ –32. mm from the sector border.

The distributions of the signal amplitudes in S2 sector, for points distanced from the sector border more than  $\sim 8$  mm, are symmetric (Gaussian) and leakage to S1 sector is negligible. The relative energy resolution  $\sigma/E$  is of the order  $\sim 2.9\%$  for 80 GeV electrons.

The dependence of the calorimeter response, leakage fraction and relative energy resolution,  $\sigma/\text{response}$ , on the distance  $d$  from the sector border, for S1 and S2 sectors are shown in Fig. 18.

Both the light output and energy resolution are a little better for S2 sector, connected to Hamamatsu PMT ( $\sigma/E \sim 2.9\%$ ), than for S1 sector, connected to Advanced Photonix APD ( $\sigma/E \sim 4.5\%$ ). This is expected since there is more light collected by the PMT as compared to the APD:  $\text{area(PMT)}/\text{area(APD)} = 1.55$ .

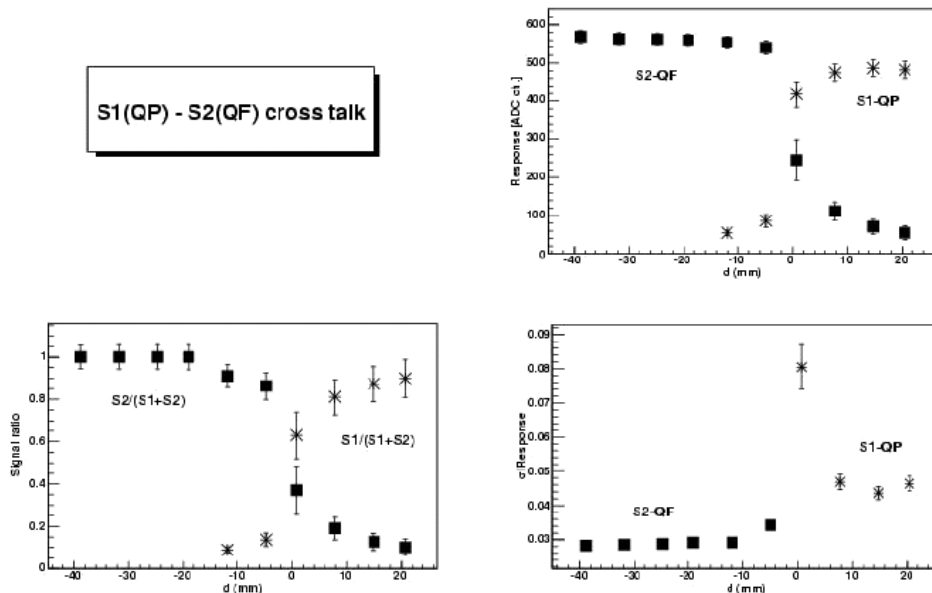


Fig.18. Comparison of the calorimeter response (top right), leakage fraction (bottom left), and relative energy resolution,  $\sigma/\text{response}$ , (bottom right) in sectors S1 (APD2) and S2 (Hamamatsu PMT) for points at different distances  $d$  from the sector border.

### 3.2.2. Comparison of J1, J2 and S1 sectors

For comparison of the uniformity of calorimeter response, several points located at different places on the sectors have been exposed to the electron beam of 80 GeV energy. The points (A–E) at the middle of J1, J2 and S1 sectors and points (4–8) at the border of S1 sector have been studied (see Fig. 2). All sectors have been connected to Hamamatsu PMT. Gaussian distributions of signal amplitudes in the middle of the sectors and asymmetric distributions close to the sector border (points 4–8) and sometimes also close to the inner (point A) and outer (point E) calorimeter edge in J1 sector are observed. The beam profile correction (aiming at selecting the central core of the impinging beam) reduces the asymmetry.

Comparison of light output and relative energy resolution for all options studied is shown in Fig. 19. Light output is highest in the S1 (QP-glass) sector and it is practically the same for the central and border points. It depends weakly on the distance  $R$  of the impact point. For S1, a weak decrease and for J1 and J2 sectors a weak increase of the calorimeter response with distance  $R$  from the calorimeter center are observed, Fig. 19. The

relative energy resolution is almost independent of the position of the impact point and it is  $\sim 1.5$ – $2.5$  % for S1 (QP-glass) and J2 (QF-glass) sectors and  $\sim 3.5$ – $4.0$  (QF-foil) for 80 GeV electrons.

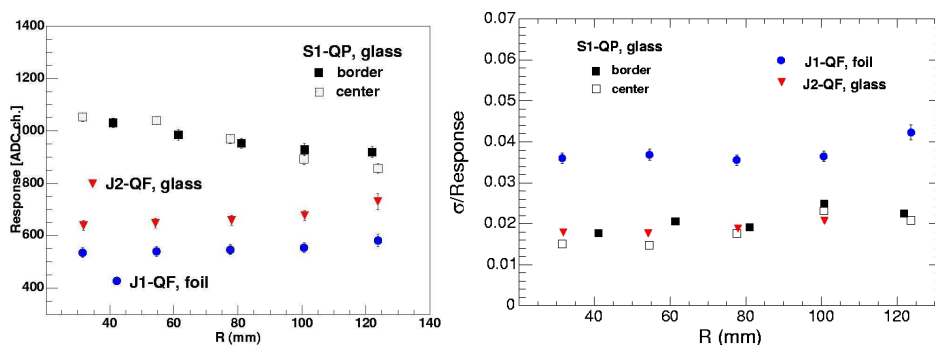


Fig. 19. Comparison of calorimeter response (left) and resolution (right) to 80 GeV electrons for several impact points (A–E) of J2, J1 and S1 sectors, readout with Hamamatsu PMTs.

#### 4. Summary

We have presented a comparative study of the performances of the first prototype of the CASTOR quartz-tungsten calorimeter of the CMS experiment using different detector configurations. **GEANT**-based MC simulations have been employed to determine the Cherenkov light efficiency of different types of air-core light guides and reflectors. Different sectors of the calorimeter have been setup with various quartz active materials and with different photodetector devices (PMTs, APDs). Electron beam tests, carried out at CERN SPS in 2003, have been used to analyze the calorimeter linearity and resolution as a function of energy and impact point. The main results obtained can be summarized as follows:

1. Comparison between the calorimeter response using a single quartz plate or using a quartz-fibre bundle indicates that:
  - (a) Good energy linearity is observed for both active medium options (Fig. 14).
  - (b) The Q-plate gives more light output than equal thickness Q-fibres (Fig. 19).
  - (c) The relative energy resolution is similar for quartz plates and quartz fibres (Fig. 15). When readout with the same Hamamatsu PMT (S1, S2 sectors), we found  $\sim 2\%$  energy resolution for 80 GeV electrons (Fig. 19).

- (d) The constant term  $p_0$  of the energy resolution, that limits performance at high energies, is less than 1% in both options for the same Philips PMT and glass reflector (Fig. 15). The stochastic term  $p_1$  is  $\sim 36\%$  and  $\sim 46\%$  for quartz plates and quartz fibres, respectively (Table VII).
- 2. Avalanche-photodiodes (APDs) appear to be a working option for the photodetectors, although they still need more investigation (radiation-hardness, cooling and voltage stabilization tests).
- 3. The relative energy resolution is weakly dependent on the position of the impact point (Fig. 19). Leakage (cross-talk) between sectors is negligible for impact points separated more than 8 mm from the sector border. Only, electrons impinging less than 3 mm from the detector edge show a degraded energy response and worse resolution.
- 4. The shape of the light guide is determined by three parameters: (i) the type of quartz fiber (NA number), (ii) the maximum efficiency and uniformity of response, and (iii) the available space for the size of a calorimeter. The aim is to simultaneously achieve optimum efficiency and uniformity of light transmission within the realistically available space. From the analysis of the MC simulations we come to the conclusion that the above requirements are best satisfied with  $lm = 0$  and  $lg = 2$  for  $NA = 0.37$  and  $0.48$ .
- 5. The light output is a little higher for the light-guides with glass reflector compared to those that use HF-foil, for the same photodetector (Hamamatsu PMT, Fig. 19). This is understood, since the HF reflecting foil is designed to cut Cherenkov light with  $\lambda < 400$  nm, where the light output is greater. However, the HF-reflector foil has higher efficiency in the region  $\lambda > 400$  nm than the glass mirror (Table VI).

In summary, this study suggests that equipping the CASTOR calorimeter with quartz-plates as active material, APDs as photodetector devices (with temperature and voltage stabilization), and light-guides with foil reflector is a promising option, although the final configuration would benefit from further (detailed) investigation to take into account the experimental conditions that will be encountered in the forward rapidity region of CMS. A beam test of the second prototype was carried out in 2004 and the results are reported elsewhere [20].

We wish to thank R. Wigmans and N. Akchurin for the assistance in the early stage of the beam test. This work is supported in part by the Secretariat for Research of the University of Athens and the Polish State Committee for Scientific Research (KBN) SPUB-M no. 620/E-77/SPB/CERN/P-03/DWM 51/2004-2006. D. d'E. acknowledges support from the 6th EU Framework Programme (contract MEIF-CT-2005-025073).

## REFERENCES

- [1] D. d'Enterria (ed.) *et al.* [CMS Collaboration], High Density QCD with Heavy-Ions. CMS Physics Technical Design Report, [CERN-LHCC 2007-009], *J. Phys.* **G34**, 2307 (2007).
- [2] J. Bartke, E. Gładysz-Dziaduś, M. Kowalski, A.D. Panagiotou, ALICE Internal Note, PHYS/93-12.
- [3] C.M.G. Lattes, Y. Fujimoto, S. Hasegawa, *Phys. Rep.* **65**, 151 (1980).
- [4] E. Gładysz-Dziaduś, *Phys. Part. Nucl.* **34**, 285 (2003), [hep-ph/0111163](#) and the references therein.
- [5] A.D. Panagiotou *et al.*, *Phys. Rev.* **D45**, 3134 (1992); M.N. Asprouli, A.D. Panagiotou, E. Gładysz-Dziaduś, *Astrop. Phys.* **2**, 167 (1994); E. Gładysz-Dziaduś, A.D. Panagiotou, Proc. Int. Symp. on Strangeness and Quark Matter (Crete), eds. G. Vassiliadis *et al.*, World Scientific 1995, p. 265; O. Theodoratou, A.D. Panagiotou, *Astrop. Phys.* **13**, 73 (2000).
- [6] E. Gładysz-Dziaduś, Z. Włodarczyk, *J. Phys. G: Nucl. Part. Phys.* **23**, 2057 (1997).
- [7] Z. Fodor, S.D. Katz, *J. High Energy Phys.* **0404**, 050, 2004 [[hep-lat/0402006](#)]; K. Rajagopal, F. Wilczek, As the Frontier of Particle Physics/Handbook of QCD, ed. M. Shifman, World Scientific 2000, Vol. 3, pp. 2061–2151.
- [8] A.L.S. Angelis, A.D. Panagiotou, *J. Phys.* **G23**, 2069 (1997); A.L.S. Angelis *et al.*, [hep-ex/9901038](#); A.L.S. Angelis *et al.*, *Nucl. Phys. Proc. Suppl.* **97**, 227 (2001); <http://cmsdoc.cern.ch/castor>
- [9] A.L.S. Angelis, J. Bartke, E. Gładysz-Dziaduś, Z. Włodarczyk, *EPJdirect* **C9**, 1 (2000).
- [10] E. Gładysz-Dziaduś [CASTOR group], Nuclear Theory'21, Rila Mountains, Bulgaria, 2002, Nuclear Theory'21, ed. V. Nikolaev, Heron Press, Sofia 2002, pp. 152–173 and the references therein.
- [11] E. Norbeck *et al.* [CMS Collaboration], *Int. J. Mod. Phys.* **E16**, 2451 (2007); E. Gładysz-Dziaduś [CASTOR group], *Acta Phys. Pol. B* **37**, 153 (2006).
- [12] M. Albrow *et al.* [CMS and TOTEM Collaborations], Prospects for Diffractive and Forward Physics at the LHC, CERN/LHCC 2006-039/G-124, CMS Note 06–5, 2006, <http://cdsweb.cern.ch/record/1005180>
- [13] M. Gyulassy, X.-N. Wang, *Phys. Rev.* **D44**, 3501 (1991); *Comput. Phys. Comm.* **83**, 307 (1994).



- [14] A.D. Panagiotou, CMS-CPT Week, PRS-HI meeting, November 2003; CMS-HF meeting, CMS Week, September 2003, CERN; see <http://cmsdoc.cern.ch/castor/Talks/Talks.html>
- [15] E. Gładysz-Dziaduś, Institute Nuclear Physics, Kraków, Report #1942 PH-2004, <http://www.ifj.edu.pl/publ/reports/2004/1942.pdf>
- [16] G. Mavromanolakis, A.L.S. Angelis, A.D. Panagiotou, ALICE/CAS-2000-27; see <https://edms.cern.ch/document/249724/1>
- [17] Ch.D. Marshall, J. Speth, S.A. Payne, *Journal of Non-Crystalline Solids* **212**, 59 (1997).
- [18] K. Deiters *et al.*, *Nucl. Instrum. Methods Phys. Res., Sect. A* **461**, 574 (2001).
- [19] G. Anzivino *et al.*, *Nucl. Instrum. Methods Phys. Res., Sect. A* **357**, 369 (1995); M. Livan, V. Vercesi and R. Wigmans, Scintillating-bre Calorimetry, CERN 95-02 (1995).
- [20] P. Katsas *et al.*, *Eur. Phys. J.* **C52**, 495 (2007).